ECS Transactions, 49 (1) 383-390 (2012)
10.1149/04901.0383ecst ©The Electrochemical Society

Hafnium aluminates deposited by atomic layer deposition: Structural characterization by X-ray spectroscopy

D.R. Huanca[a], V. Christiano[a], C. Adelmann[b], G. Kellerman[c], P. Verdonck[b] and S.G. dos Santos Filho[a]

[a]LSI/PSI/EPUSP, Av. Prof. Luciano Gualberto,158, 05508-900 São Paulo, SP, Brasil,
[b]IMEC, Kapeldreef 75, B-3001 Leuven, Belgium
[c]UFPr, Av Cel Francisco H. dos Santos, CEP81531990,Curitiba, PR, Brasil – C.P. 19044

Hafnium aluminates thin films deposited (50% Hf) by atomic layer deposition upon silicon substrate and then annealed by two different methods into two different environments. Their structural and chemical behaviors after thermal treatment were investigated using X-ray spectroscopy. For thin films annealed at 1000 ^{o}C for 60 s in N_2, phase separation take place, promoting the formation of HfO_2 spheroidal crystalline nanoparticles embedded in $Al_{2.4}$ $O_{3.6}$, while in that annealed by laser HfO_2 remains in its amorphous phase, but the aluminum oxide crystallizes in $Al_{2.4}O_{3.6}$ forming spheroidal nanoparticles.

Introduction

The scaling down of CMOS devices requires the substitution of silicon oxynitride as gate dielectric because the dielectric properties of latter dielectric lose its electrical properties when it achieves about 3 nm of thickness (1-3). In order to overcome this difficulty, different high-*k* dielectric composed by binary and ternary compounds were proposed and used (1-3). One, which belongs to these set of high-k dielectric, is the hafnium oxide (HfO_2) that was deposited on a silicon substrate using different methods such as sputtering, atomic layer deposition (ALD), metalorganic chemical vapor deposition, pulsed laser and so on (1,3-6). Although the HfO_2 has a high dielectric constant ($k \approx 20$), this material crystallizes at relatively low temperature (≈ 500 ºC) (7,8). Crystalline HfO_2 is undesirable because promotes an unstable silicon/metal oxide interface due to the electric and mass transfer (9) as well as the coexistence of different crystalline phases give rise to anisotropy of the dielectric constant along the whole structure (10,11). In order to maintain the HfO_2 in its amorphous phase even during thermal treatment in CMOS processing, different strategies have been employed such as adding SiO_2 (1,12) or Al_3O_2 during the deposition (1,9,13-14). On the other hand, structural characterization of thin films requires complementary techniques such as scanning electron microscopy, transmission electron microscopy (TEM) (9,13), Rutherford backscattering spectroscopy (15) and those based in X-ray spectroscopy (16-19). The grazing incidence scattering X-ray spectroscopy (GISAXS) belongs to the latter set of characterization techniques and permits to determine both shape and size of nanoparticles embedded in the thin film (17,19). In this paper we report the structural and chemical characterization of HfAlOx thin films deposited by ALD method and then annealed. The characterization was made by X-ray reflectance (XRR), GISAXS and grazing incidence X-ray diffraction (GIXRD).

Experimental Procedure

We deposited one set of hafnium aluminates on silicon substrate by atomic layer deposition ALD technique to obtain equal molar concentrations of 50% for hafnium and aluminum. Following, the films deposited were annealed at 1000 ºC for 60s in ultrapureN_2 (sample D08) and N_2+5% O_2 (sample D11). One sample (D10) was annealed by laser in N_2 for similar time. Structural features of these thin films were characterized using XRR and GISAXS whereas their chemical features were investigated using GIXRD technique. The labels as well as the annealing condition of these samples are summarized in Table 1. The XRR as well as GISAXS spectra were recorded focusing X-ray beam with wavelength λ= 1.749 Å and, in the case of GISAXS, the incidence angle was 0.5º. The GIXRD analysis were carried out with λ= 1.542 Å at 0.7º. GISAXS pattern was analyzed by the IsGISAXS code placing into the program the refractive index, surface roughness and layer thickness obtained from XRR spectra.

Table 1. Annealing conditions and structural parameters of hafnium aluminates analyzed here.

Sample	Environment	Annealing method	Thickness (nm)	Surface Roughness (nm)	Interface Roughness (nm)	Critical angle
D08	N_2	Furnace	28.8	0.90	0.50	0.4141
D10	N_2	Laser	29.0	0.85	0.20	0.4297
D11	N_2+5% O_2	Furnace	28.5	1.3	1.0	0.4128

Results and discussion

Structural analysis by X-ray reflectance

The XRR curves in Figures 1a-1c show the wavy appearance (Kiessig fringes) due to the interference effect of the beams reflected at the air/dielectric and dielectric/silicon interfaces (17,20). The periodicity of these undulations is linked to the dielectric thickness, while slope is related to the roughness of both interfaces (16-18,20). These curves were fitted using a single layer model given by the equation 1 (17)

$$R = \frac{r_{0,1}^2 + r_{1,2}^2 + r_{0,1}r_{1,2}\cos(q_z t)}{1 + r_{0,1}^2 r_{1,2}^2 + r_{0,1}r_{1,2}\cos(q_z t)} \quad [1]$$

$$r_{i,i+1} = r_{i,i+1}^{flat} e^{-q_{z,i}q_{z,i+1}\sigma_i^2/2} \quad [2]$$

Where t is the thickness of the dielectric layer, $r_{i,i+1}$ is the beam reflectivity at the interface between two near layers. The cosine term in equation 1 arises from the interference effect of the x-ray beam reflected at both interfaces. The reflectivity $r_{i,i+1}$ includes the term with the effect of the interface roughness times the reflectance value expected in a smooth layer (equation 2) (17).

It was found that the thickness of these dielectric films varies from 28.5 to 29.0 nm, although they were deposited under the same conditions (Table 1). However, the surface and interface roughness are different and depend on the annealing conditions. The surface roughnesses vary from 0.85 to 1.3 nm and are compatible to that reported by Nishimura et al. (9). According to these authors, this roughness arises from the decomposition of hafnium aluminate into HfO_2 and Al_2O_3. Concerning the roughness of both air/film (1.3 nm) and film/silicon (1.0 nm) interfaces of the thin film annealed in N_2+5% O_2 (D11) that are larger compared to the other films, it is clear that the oxygen addition into the annealing environment increase the hafnium aluminate decomposition since this roughness is lower in the film annealed in N_2 environment (D08) and, exhibits lower surface and interfacial roughness (Table 1). The lowest roughness was observed for the

films annealed by laser in N_2 (D10). Furthermore, the fit of these curves also reveals that they have slightly different critical angles varying from 0.4128º to 0.4297º (Table 1) and showing that laser annealing process promotes thin films with superior dielectric constant since both critical angle and dielectric constant are intimately correlated (20,21).

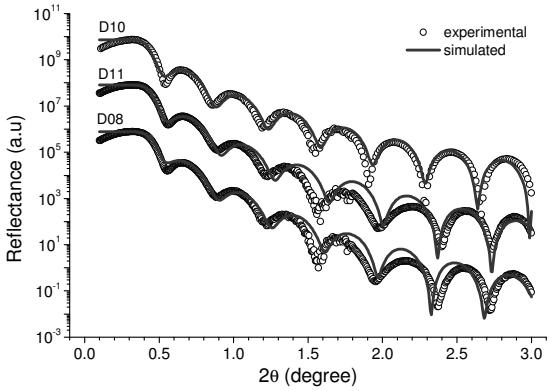

Figure 1. X-ray reflectance of samples annealed in N_2 (D08), N2+5% O_2 (D11) and by laser (D10).

Structural analysis by Grazing incidence X-ray Scattering

As commented before, unfortunately the most promising candidate to substitute the silicon oxinitride as gate oxide becomes crystalline during the CMOS processing (7,8) and to overcome this problem SiO_2 or Al_2O_3 were added (1,12-14). However, depending on the deposition conditions or post-deposition treatments, phase separation can occur, giving rise to the formation of nanoparticles into the dielectric film (12,13). In this sense, a powerful tool for characterizing these nanoparticles is the GISAXS method (12,19). Thus, complementary information about the structural features of these samples will be extracted from GISAXS pattern shown in Figures 2a-2c, whose similitude among them is noticeable. Only a slight difference occurs for that corresponding to the film annealed by laser (D10) in the diffuse region (defined by dashed lines). This fact shows that the distribution of nanoparticles formed in this film is more anisotropic (17,19) than in the others and, therefore, they are more polydispersive . Additionally, the characteristic Yoneda peak (22) is observed in these GISAXS patterns. The position of this peak is correlated with the critical angle of the dielectric film and arises due to the complete reflection of the beam (17,19). Prior to analyze the GISAXS patterns with IsGISAXS program (23), these spectra were cut in 10 parts in order to estimate the mean nanoparticle shape into the dielectric layer. For this aim, it were used the Guinier relation and its modified form for elongated and flatted nanoparticles (24). The general Guinier relation can be written as:

$$\ln(q_y^n I) = A + \frac{R_g^2}{3-n} q_y^2 \qquad [3]$$

Where n = 0 for spheres, 1 for elongated, and 2 for flatted nanoparticles. R_g is the gyration radius of the sphere, or gyration radius of cross-sectional (R_c) of the elongated or flatted (R_t) nanoparticles, respectively. According to the results shown in Figures 2d-2f the system seems to be monodispersive composed by elongated nanoparticles because they exhibits a linear behavior, except for sample D10 in which the system looks like to be composed by flatted nanoparticles mainly in deeper regions where they are dominant since the linear behavior of first cuts appear only when $\ln(q_y^2 I)$ versus q_y^2 is plotted

revealing thus the predominance of flatted nanoparticles (Figure 2b), whereas in upper regions the system could be composed by elongated particles (inset in Figure 2e). This behavior of this film reveals that the system is composed by nanoparticles with complex form that could be similar to that observed by Stemmer et al (12) for hafnium oxide films mixed with 40% of silicon oxide. In addition, since the slope of these curves varies as function of the cut (or equivalently as function of q_z), it is clear that the nanoparticle size and also its polydispersion (in the case of sample D10) increase in-depth.

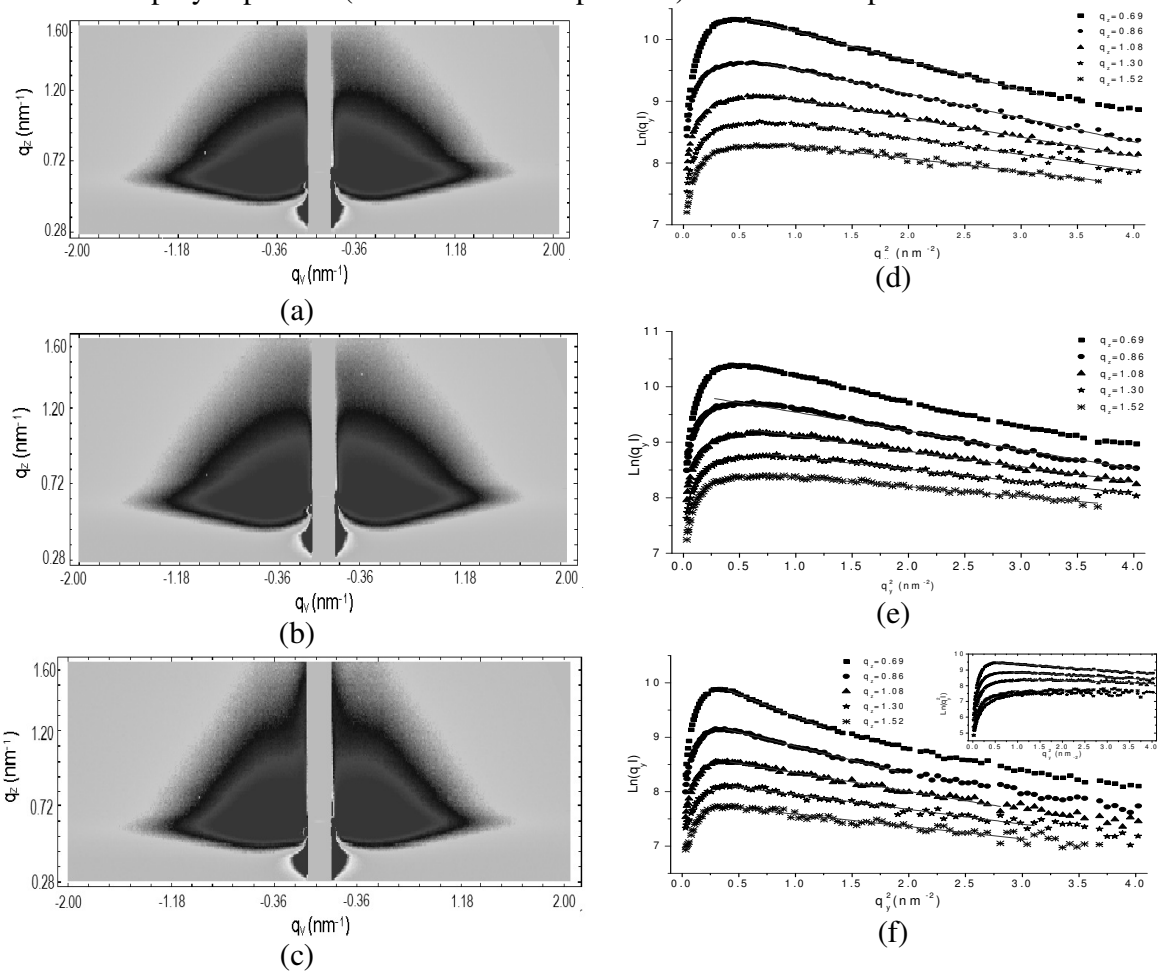

Figure 2. GISAXS pattern from thin films annealed in N_2 (a), N_2+5% O_2 (b), and by laser (c). Their respective modified Guinier plots for elongated nanoparticles are in (d), (e) and (f), respectively. Inset of (f) it is shown the Guinier plot for flatted nanoparticles.

Assuming the nanoparticles, embedded in all samples, have spheroidal shape, we can estimate roughly their cross-section radius R_c from equation 3 with n = 1, while their length are estimated through the relation $L = \sqrt{12R_g^2 - 6R_c^2}$ where R_g is obtained using the Guinier plot $\ln(I)$ versus q_y^2 (equation 3 with n= 0). The results are plotted in Figure 3 and shows that spheroidal nanoparticles with larger R_c are localized in low q_z regions whereas L are also larger for samples annealed in N_2 and N_2+5% O_2, respectively. On the other hand, larger spheroids with greater lengths were formed within thin film annealed by laser.

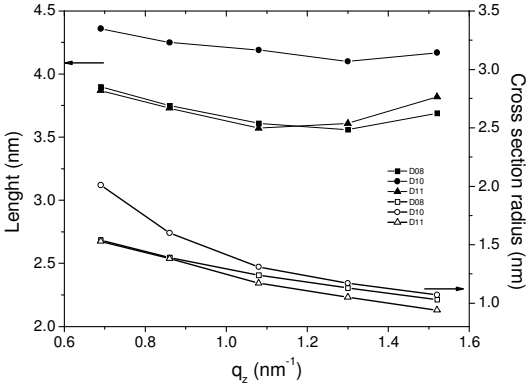

Figure 3. Cross-section and length of nanoparticles embedded into the thin films annealed in N_2 (square), N_2+5% O_2 (triangle), and annealed by laser (circle). The cross-section is represented by unfilled symbols and the length by filled.

Based on the results presented in Figure 3, we fitted the GISAXS pattern supposing that the nanoparticles had cylinder or prolate spheroid shapes. Usually, nanoparticles embedded in the layers are fitted by supposing spheres distributed following a Gaussian or normal distribution (25,26) and, sometimes the log-normal distribution (27). However the nanoparticles investigated here were better fitted using spheroids together the Lorentz-Cauchy distribution (equation 4).

$$N(R) = \left\{ \pi(\sigma / R_0) \left[1 + \left(\frac{R / R_0}{\sigma / R_0} \right)^2 \right] \right\}^{-1} \quad [4]$$

Nonetheless, it is important to emphasize that nanoparticle can have more complex shape depending on the HfO_2/Al_2O_3 ratio and post-deposition thermal treatment (12,13). In the GISXS theory, the scattering intensity from nanoparticles embedded into a medium depends on the electron density contrast ($\Delta\rho=\rho_n-\rho_m$) as well as on a form factor *F(q)* times the structure factor *S(q)*. For a highly monodispersive system, the effective surface approximation the scattered intensity can be written as (17,19):

$$I = \frac{A\pi^2}{\lambda^4} (\Delta\rho)^2 |T_i|^2 |T_f|^2 \int F(q) S(q) N(R) dR \quad [5]$$

Where A is the illuminated surface area, $T_{i,f}$ are the Fresnel transmissions functions for incident and reflected beams, *N(R)dR* is the number of particles embedded into the layer. In the case of samples investigated here, they were well fitted using the Lorentzian distribution with the form factor of spheroids given by equation 6 (17,19).

$$F(q) = \exp(iq_z H/2) \int_0^{H/2} 4\pi R_z^2 \frac{J_1(q_\parallel R_z)}{q_\parallel R_z} \cos(q_z z) dz \quad [6]$$

Where the term $J_1(q_\parallel R_z)$ is the Bessel function of first order, $q_\parallel = \sqrt{q_x^2 + q_y^2}$ is the lateral wave transfer vector and $R_z = R\sqrt{1+(2Z/H)^2}$. Results obtained by fitting the GISAXS spectra are summarized in Table 2. The values in parenthesis correspond to oblate spheroids and the other belongs to prolate spheroids. Figure 4a shows a one-dimensional GISAXS pattern fitted by IsGISAXS code, revealing also the isometric lack in intensity, especially for the low qz region while for the high q_z regions, the spectra are almost symmetric. This behavior was observed for all samples and could be attributed to effect of complex nanoparticle shape with fractal features in deeper regions due to the higher

aggregation. The complexity of the nanoparticle shape is lower in the high q_z region in which the nanoparticles are small (24).

Table 2. Dimensions of spheroid nanoparticles embedded in all dielectric films.

sample	σ_R/R	σ_H/H	R(nm)	H(nm)	D(nm)	cut-off
D08	0.05-0.11	0.05-0.1	1.3-1.8	1.9-2.6	14-19	8.5-14.5
D10	0.15-0.2;(0.08)	0.05-0.12	1.0-1.8;(1.6)	1.6-2.1;(1.3)	10.5-13.0;(10.5)	7.0-7.5;(8)
D11	0.07-0.1	0.05-0.13	1.6-2.0	1.6-2.3	11-13.5	5.5-9.0

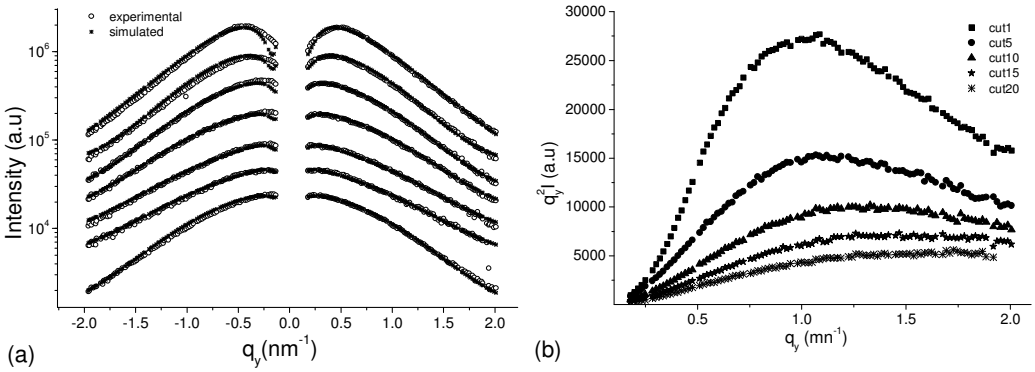

Figure 4. (a) One-dimensional GISAXS pattern of thin film annealed in N_2 environment fitted by IsGISAXS program; and (b) its correspondent Kratky plot for five cuts along the thin film.

According to the Table 2, the R values obtained by IsGISAXS code are slightly different than that (R_c) obtained by modified Guinier relation. However, length-values are almost twice than H-values. It can be attributed to the complex geometry of the elongated nanoparticles. Similar values were observed for the sample annealed in N_2 as well as, for the one annealed in N_2+5% O_2. Additionally, for the case of the dielectric layer annealed by laser (D10), oblate nanoparticles are also formed during the annealing process (values in parenthesis in Table 2) and they are predominant in high q_z regions. The results reported here are compatible with prior works reported by Stemmer et al. (12,13) who observed that nanoparticles with almost spheroidal shape are formed in HfO_2-Al_2O_3 or HfO_2-SiO_2 systems. The size and complexity of these particles depends on the HfO_2 concentration (12,13). The geometrical complexity level of these nanoparticles can also be seen in Kratky plot (Figure 4b). Since the $q_y^2 I - q_y$ curves in low q_z regions have parabolic format which becomes distorted as q_z grows, this can be understood as nanoparticles that change their shape along the film thickness being it elongated in regions near to the thin film surface to almost spherical with mass fractal in regions closer to film/silicon interface. Parabolic Kratky plot is attributed to sphere-like nanoparticles whereas when it tends to be constant at high q_y values, the nanoparticle can have a roughly elongated shape also known as Gaussian chain (24). Similar behavior was observed for all the samples, although between them are some significant differences especially between those annealed in N_2 and that annealed by laser (Figure 5a). The maximum point of both films annealed in N_2-based environment are localized at almost same position in Figure 5a as well as their shape are similar revealing that nanoparticles with similar geometrical features are formed, results that are compatible with Guinier (Figure 3) and IsGISAXS analysis (Table 2). However, for the film annealed by laser (D10) the maximum point is shifted toward low q_y regions attributed to nanoparticles

with larger Rc, as shown by the Guinier analysis (Figure 3). Its shape is less like than a parabola, being it more similar to that shown by a rough elongated nanoparticle with mass fractal, as was shown by Guinier and IsGISAXS analysis.

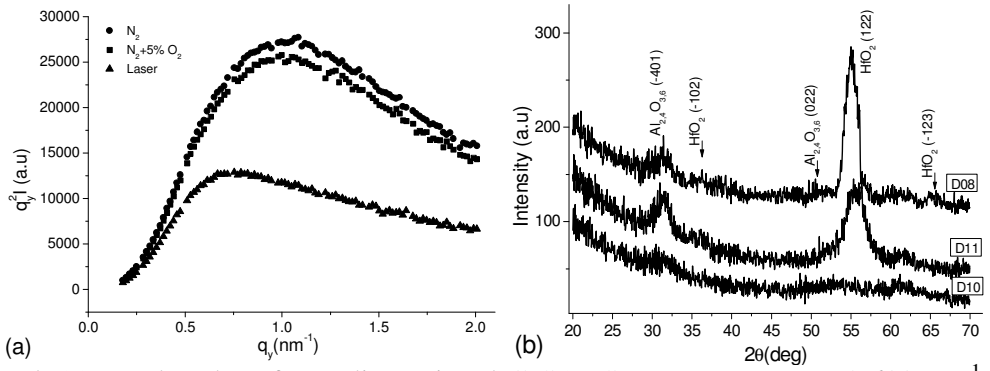

Figure 5. (a) Kratky plot of one-dimensional GISAXS pattern cut at q_z=0.688 nm^{-1}(cut1) of dielectric films annealed in N_2 (D08) and N_2+5%O_2 (D11) and laser (D10); and (b) their corresponding GIXRD, respectively.

Grazing incidence X-ray diffraction analysis

The chemical characterization by GIXRD (Figure 5b) shows that in the films annealed in N_2 and N_2+O_2(5%) the films are composed by crystalline $Al_{2.4}O_{3.6}$ and HfO_2. For the film annealed in N_2 (D08), the largest peak in $2\theta \approx 55^{\circ}$ suggest the formation of largest number of nanoparticles than that annealed in N_2+5%O_2 (D11); the lower peak of GIXRD of the latter film indicates lower concentration of nanoparticles formed while its larger full width at half maximum (FWHM) points out that the nanoparticles are slightly larger, as shown by IsGISAXS analysis (Table 2). Moreover, the larger peak in $2\theta \approx 31.5^{\circ}$ shows that the addition of 5%O_2 in the media increases the formation of crystalline phase of $Al_{2.4}O_{3.6}$, thus the system can be interpreted as HfO_2 nanoparticles embedded in $Al_{2.4}O_{3.6}$ film, similar to that observed for hafnium aluminates and hafnium silicates (12,13). On the other hand, the absence of HfO_2 peaks in the GIXRD spectrum of the sample annealed by laser shows that this compound remains in its amorphous phase; therefore the system can be interpreted as $Al_{2.4}O_{3.6}$ nanoparticles embedded in amorphous medium. It could explain the lowest intensity of its GISAXS spectrum (Figure 5a) since it is strong dependent on the nanoparticle concentration, as shown by equation 5.

Conclusions

Hafnium aluminates films annealed in different environments were investigated by X-ray spectroscopy methods. The results showed that for thin films annealed in N_2-based media, HfO_2 nanoparticles with spheroid shape embedded within crystalline $Al_{2.4}O_{3.6}$ are formed whereas in that annealed by laser, the HfO_2 remains in an amorphous phase, even though that low quantities of crystalline $Al_{2.4}O_{3.6}$ is also present. The GISAXS analysis of these samples indicates that spheroidal nanoparticles are formed in this latter thin film, however additional analysis using Kratky plot reveals that these nanoparticles have complex geometry and also have fractal mass. Additionally, different to prior works reported by different authors (25-27), the GISAXS pattern of these particles are well fitted by Lorentz distribution. From gate dielectric point of view, the annealing process by laser is more suitable because in this film the HfO_2 remains amorphous even after 60 second of annealing, making this procedure suitable for CMOS processing.

Acknowledgments

The authors thank FAPESP for financial supports and to the LNLS for equipment facilities.

References

1. J. Robertson, *Rep. Prog. Phys.,* **69**, 327 (2006)
2. M. T. Bohr, R. S. Chau, T. Ganhi, and K. Mistry, *IEEE Spec*., **30** (2007)
3. M. Houssa, High-k gate materials, p. 4, Institute of Physics Publishing, U.S.A (2004)
4. R. J. Potter, P. A. Marshall, P. R. chalker, S. Taylor, A. C. Jones, T. C. Q. Noakes, and P. Bailey, *App. Phys. Let.,* **84**, 4119 (2004)
5. A. Delabie, R. L. Puurunen, B. Brijs, M. Caymax, T. Conard, B. Onsia, O. Richard, W. Vandervorst, C. Zhao, M. M. Heyns, M. Meuris, M. M. Viitanen, H. H. Brongersma, M. de Ridder, L. V. Goncharova, E. Garfunkel, T. Gustafsson, and W. Tsa, *J. App. Phys*., **97**,064104 (2005)
6. A. C. Jones, H. C. Aspinall, P. r. Chalker, R. J. Potter, T. D. Manning, Y. F. Loo, R. O'Kane, J. M. Gaskell, and L. M. Smith, *Chem. Vap. Deposition*., **12**, 83 (2006)
7. M.-Y. Ho, H. Gong, G. D. Wilk, B. W. Busch, M. L. Green, P. M. Voyles, D. A. Muller, M. Bude, W. H. Lin, A. See, M. E. Loomans, S. K. Lahiri, and P. I. Raisanen, *J. App. Phys.,* **93**, 1477 (2003)
8. E.P. Gusev, C. Cabral Jr., M. Copel, C. D'Emic, M. Gribelyuk, *Microelectron. Eng*., **69**, 145 (2003)
9. T. Nishimura, T. Okazawa, Y. Hoshino, Y. Kido, K. Iwamoto, K. Tominaga, T. Nabatame, T. Yasuda, and A. Toriumi, *J. App. Phys.,* **96**, 6113 (2004)
10. N. Mommer, T. Lee, and J. A. Gardner, *J. Mater. Res*., **15**, 377 (2000)
11. X. Zhao, and D. Vanderbilt, *Phys. Rev. B.,* **65**, 233106 (2002)
12. S. Stemmer, Y. Li, S. K. Streifer, P. Fuoss, and S. Seifert, *Appl. Phys. Lett.,* **83**, 3141 (2003)
13. Y. Yang, W. Zhu, T. P. Ma, and S. Stemmer, *J. App. Phys.,* **95**, 3772 (2004)
14. T. Wang, and J. G. Ekerdt, *Chem. Mater.,* **23**, 1679 (2011)
15. U. M. Bhatta, J. Ghatak, M. Mukhopadhyay, R. Conley, Ch. Liu, and P. V. Satyam, *Nucl. Inst. Meth. Phys. Reser. B*., **266**, 1548 (2008)
16. C. Wyon, J. P. Gonchond, D. Delille, A. Michallet, J. C. Royer, L. Kwakman, and S. Marthon, *Appl. Surf. Sci.,***253**, 21 (2006)
17. R. Lazzari, X-ray and Neutron Reflectivity: Grazing Incidence Small-Angle X-ray Scattering from Nanostructures, edit. J. Daillant, A. Gibaud, Springer, Berlin (2009)
18. S. Terada, H. Mrakami, K. Nishihagi, and H. Osaka, IEEE/SEMI: Advanced Semiconductor Manufacturing Conferences, 125, (2001).
19. P. Müller-Buschbaum, A Basic Introduction to Grazing Incidence Small-Angle, in Applications of Synchrotron Light to scattering and Difraction in Materials and Life Science, edit. M. Gomez, A. Nogales, M. C. Garcia-Gutierrez, and T. A. Ezquerra, Springer, Berlin (2009)
20. U. Pietsch, V. Holy, and T. Baumbach, High-Resolution X-ray Scattering: From thin Films to Lateral Nanostructures, p.143, Springer-Verlag, New York (2004).
21. A. Gibaud, and G.Vignaud, X-ray and Neutron Reflectivity: Specular Reflectivity from Smooth and Rough Surfaces, edit. J. Daillant, A. Gibaud, Springer, Berlin (2009)
22. Y. Yoneda, *Phys. Rev*., **131**, 2010 (1963)
23. R. Lazzari, *J. Appl. Cryst*., **35**, 406 (2002)
24. G. Glatter, and O. Kratky, Small Angle X-ray Scattering, Academic Press, New York (1982)
25. V. Christiano, C. Adelmann, G. Kellermann, P. Verdonck, and S. G. dos Santos Filho*, ECS trans.,* **39,** 393 (2011)
26. M. Krumrey, G. Gleber, F. Scholze, and J. Wernecke, *Meas. Sci. Technol.,* **22**, 094032 (2011)
27. J. R. Casanova, E. A. Heredia, C. D. Bojorge, H. r. Cánepa, G. Kellermann, and A. F. Craievich, *App. Sur. Sci.,* **257**, 10045 (2011)